Electrochimica Acta 525 (2025) 146094

Contents lists available at ScienceDirect

Electrochimica Acta

journal homepage: www.journals.elsevier.com/electrochimica-acta

Hemp stem derived platinum metal-free electrocatalysts for oxygen reduction reaction in alkaline electrolyte

Leire Caizán-Juanarena [a], Matteo Boventi [b], Mohsin Muhyuddin [b], Stefano Caporali [c], Enrico Berretti [d], Alessandro Lavacchi [d], Antunes Staffolani [e,f], Michele Mauri [b], Roberto Simonutti [b,*], Carlo Santoro [b,*]

[a] Departamento de Física Aplicada I, Universidad de Málaga, 29071 Málaga, Spain
[b] Department of Materials Science, University of Milano-Bicocca, U5 building, Via Cozzi 55, 20125 Milan, Italy
[c] Department of Industrial Engineering, University of Florence, Via Di Santa Marta 3, 50139 Florence, Italy
[d] Istituto di Chimica Dei Composti Organometallici (ICCOM), Consiglio Nazionale Delle Ricerche (CNR), Via Madonna Del Piano 10, 50019 Sesto Fiorentino, Firenze, Italy
[e] Department of Chemistry "Giacomo Ciamician", Alma Mater Studiorum University of Bologna, 40129 Bologna, Italy
[f] ENERCube, Centro Ricerche Energia, Ambiente e Mare, Centro Interdipartimentale per la Ricerca Industriale Fonti Rinnovabili, Ambiente, Mare ed Energia (CIRI-FRAME)—Alma Mater Studiorum University of Bologna, Viale Ciro Menotti, 48, 48122 Marina di Ravenna, Italy

ARTICLE INFO

Keywords:
Hemp waste
Biochar production
^{129}Xe NMR
PGM-free electrocatalyst
oxygen reduction reaction

ABSTRACT

This study focuses on the synthesis of low-cost platinum group metal-free (PGM-free) electrocatalysts for the oxygen reduction reaction (ORR) in alkaline media. With that purpose, hemp stem derived products referred to as fibers (HF) and shives (HS), commonly waste by-products of the textile industry, are used as readily available carbon sources that are transformed into conductive char through pyrolysis. Three pyrolysis temperatures are investigated (400, 600 and 800 °C). Subsequently, the char is chemically activated and functionalized with iron azamacrocyles to obtain Fe-Nx-C defect-rich porous structures with the desired distribution of active moieties in a porous architecture. The influence of the raw material on the physicochemical properties and electrochemical performance of the electrocatalysts is thoroughly examined. ^{129}Xe NMR indicates carbonaceous porous structures in the mesoporous range, mainly created in the activation process. XRD reveals amorphous carbon signals and iron oxide-related peaks in the synthesized materials, while Raman spectroscopy shows defect-rich architectures that favor ORR. Additionally, XPS confirms the coexistence of various nitrogen and iron-containing active moieties and SEM-EDX images show homogeneously distributed iron particles with little formation of clusters. All electrocatalysts demonstrate significant ORR activity under alkaline conditions; the highest performance is achieved by the sample HF600 in terms of E_{on} and $E_{1/2}$, with values of 0.97 and 0.92 V vs RHE, respectively. This research presents a promising route towards a cost-effective production of PGM-free ORR electrocatalysts with an upgrading of waste biomass for environmentally friendly energy applications.

1. Introduction

Sustainability and technological rationality are the two core determinants to mitigate the surging crises of the 21st century, at the foremost are dramatic population growth, severe energy shortfall, alarming extinction of fossil fuels and unprecedented environmental degradation. Combining the themes of 'Circular Economy' and 'Hydrogen Economy', the aforementioned objectives can be aimed at effectively. Circular Economy fosters re-employment and re/upcycling of the phased-out products that could also help in minimizing waste generation and convincingly depressing the financial deficit. On the other hand, the Hydrogen Economy presents green hydrogen as a novel energy vector ensuring the curtailment of carbon footprints along with negligible greenhouse gas emissions. Hydrogen as a green and sustainable fuel can be used in low-temperature fuel cells (FCs), i.e. proton exchange membrane fuel cells (PEMFCs) and anion exchange membrane fuel cells (AEMFCs), for the continuous and efficient translation of chemical energy into electrical energy for mobile, domestic and

* Corresponding authors.
E-mail addresses: roberto.simonutti@unimib.it (R. Simonutti), carlo.santoro@unimib.it (C. Santoro).

https://doi.org/10.1016/j.electacta.2025.146094
Received 14 January 2025; Received in revised form 12 March 2025; Accepted 21 March 2025
Available online 24 March 2025

industrial applications [1].

Despite unparalleled advantages, their broad-reach deployment is still restricted due to the utilization of scarce and overpriced platinum group metals (PGMs) for electrocatalyst fabrication. Compared to the anode-side hydrogen oxidation reaction (HOR), the complex kinetics of oxygen reduction reaction (ORR) occurring at the cathode are slower with several orders of magnitude, and relies on much higher Pt loading [2,3] that contributes up to ca. 56 % of the total cost of the membrane electrode assembly [4]. Therefore, the ORR constitutes the core bottleneck in the commercial realization of FC technology by challenging its economic feasibility. In the pursuit of PGM-free ORR electrocatalysts, carbon-based nanomaterials, importantly transition metal-nitrogen-carbons (M-N_x-Cs), are evolving as promising candidates in which carbon acts as a robust matrix and provides the conducting platform for the ORR [5–7].

The development of carbon-based M-N_x-Cs utilizing agricultural and industrial biomass waste is a hot research topic, closely aligned with the principles of circular economy [8]. Besides, scalable industrial production of state-of-the-art carbon-based nanomaterials like graphene and nanotubes is also limited by the cost spikes. On the flip side, the annual global production of biomass waste is surpassing 140 billion metric tons [9]. The transformation of waste biomass into carbonaceous nanomaterials for energy conversion and storage applications not only provides an alternative and cost-effective pathway, but also promotes eco-friendly solutions over traditional waste management methods like incineration and landfilling that typically raise ecological concerns [10]. Therefore, in recent times many endeavors have been made to valorize waste biomasses and plastics into carbon-based M-N-Cs [11, 12], such as pistachio shells [13], lignin [14], fruit peels [15,16] or cigarettes [17,18] which are usually outside the conventional recycling routes.

Among various biomasses, hemp is a spring-flowering and wind-pollinated plant with a high annual yield [19] and can be harvested in most regions due to its weather-resistant nature [20]. As per a recent report by the European Commission, in 2022 the agronomic output of hemp within the EU had increased by 84.3 % (reaching 179,020 tons) over the last seven years and, in the same year, it was cultivated on >33, 020 hectares with a 60 % increment from 2015 to 2022 [21]. Moreover, acknowledging the economic worth and suitability of hemp for diverse applications, including the textile industry, the US and EU have withdrawn the restrictions on hemp cultivation and thereby this sector is expected to expand progressively [22]. Nevertheless, it is important to highlight that, owing to complex physiochemical properties and structure, hemp cannot undergo an easy decomposition and therefore it always requires definitive pre-treatments [23,24]. However, the hemp components i.e. fibers and shives are mainly composed of lignocellulosic constituents [23], which can produce good quality porous biochar that can be used as a cost-effective precursor for electrocatalyst development [25].

Lately, scientific interest has been witnessed in hemp-derived nanomaterials for green energy applications and, particularly, the ORR electrocatalysts. Not long ago, Marrot et al. reported the thermal transformation of hemp into highly electroconductive biochar at 800–1000 °C [26]. Similarly, Antorán et al. valorized waste hemp into porous carbon through pyrolysis and chemical activation that exhibited encouraging performance after being applied as an anode in sodium-ion batteries [27]. In the same vein, Tekin and Topcu synthesized hemp-derived activated carbon for cathode applications in an aqueous zinc-ion hybrid supercapacitor that delivered notable cycling stability up to 2000 cycles [28]. Recently, Zhang and coworkers prepared Co/N doped porous nanostructured carbon after $NaHCO_3$ activation for ORR electrocatalysis that exhibited appreciable half-wave potential ($E_{1/2}$) of 0.82 V (vs RHE) in the alkaline media, along with satisfactory methanol tolerance [29]. It is noteworthy that Co has been listed as a critical raw material (CRM) [30] and may also induce toxic or carcinogenic effects [31]. On the other hand, Fe is always considered the metal of choice while fabricating M-N-Cs for ORR due to its suitable electronic structure of iron that allows favorable thermodynamic interaction with oxygen [7, 32,33]. Moreover, when Fe is present in coordination with nitrogen, it biomimics natural enzymes to carry out ORR in a four-electron fashion [7].

In this study, hemp-derived Fe-N-C-type electrocatalysts were developed for ORR applications in the alkaline media. Specifically, Fe-based PGM-free ORR electrocatalysts were synthesized for the first time from hemp shives (HS) and fibers (HF) as separate substrates. Pursuing different pyrolysis temperatures, all electrocatalysts have been characterized with multiple physicochemical and electrochemical techniques, specifically for the reduction of oxygen.

2. Material and methods

2.1. Synthesis of electrocatalysts

The hemp stem is composed of bast fibers encircling the woody hemp core, also referred to as hemp shives. These two parts, having different morphology and composition, were first separated manually. Raw materials can be seen in Fig. 1, where the synthesis process of electrocatalysts is also summarized: 1) pyrolysis, 2) chemical activation and 3) functionalization.

Both substrates (HS and HF) were dried at 80 °C overnight and then ground to a fine powder using a common coffee grinder. Afterward, the three powder samples from each category were separately pyrolyzed for 1 h at three different temperatures, 400, 600 and 800 °C (Nabertherm furnace), at a heating and cooling ramps of 5 °C min^{-1} and a controlled N_2 atmosphere, with a feeding rate of 100 cm^3 min^{-1}.

The produced chars were activated following the method reported by Lv et al. [34] Each pyrolyzed product was ground and poured inside a round bottom flask containing solid KOH diluted in 30–40 mL of ethanol, maintaining a weight basis proportion of 4:1 between the KOH and carbon, respectively. It was stirred overnight at 250 rpm, keeping the flask closed to avoid ethanol evaporation. The day after, the liquid was evaporated with a heating plate at 80 °C under nitrogen flux, and the dried powder was placed in ceramic boats for further heat treatment. To avoid a chemical reaction between the KOH and the silica boats, the latter ones were covered with nickel stripes. The activation process of the carbon powder to enhance porosity was then performed at 700 °C for 1 h, at heating and cooling ramps of 5 °C min^{-1} and a controlled N_2 atmosphere (100 cm^3 min^{-1}). Thereafter, acid washing was performed with a 1 M HCl solution to remove KOH from the activated carbon, which was then repeatedly rinsed with milli-Q water under vacuum filtration until neutral pH was achieved. The obtained powders were dried overnight in an oven.

To functionalize all six samples, each activated powder was carefully mixed with iron phthalocyanine (FePc) in a weight basis proportion of 80–20 %, respectively, and then heat treated at 600 °C for 1 h, with heating and cooling ramps of 5 °C min^{-1} and a controlled N_2 flux of 100 cm^3 min^{-1}. The resulting electrocatalysts are named HS400, HS600 and HS800 for hemp shives and HF400, HF600 and HF800 for hemp fibers, with numbers referring to the related pyrolysis temperatures.

2.2. Physicochemical characterization of the electrocatalysts

2.2.1. Structural and morphological characterization

To assess the crystal structure of the synthesized electrocatalysts in carbon powder form, X-ray diffraction (XRD) was conducted over a 2θ range of 10 to 80° using a Rigaku Miniflex 600 instrument with a copper source.

Similarly, to analyze the carbonaceous structure of samples, Raman spectroscopy was employed using a LabRam system (Jobin Yvon, France). The system utilized a helium-neon laser (λ = 632.8 nm) as the excitation source, focused on the sample with the aid of an Olympus BX40 microscope (Japan) and a silicon-based CCD detector (Sincerity,

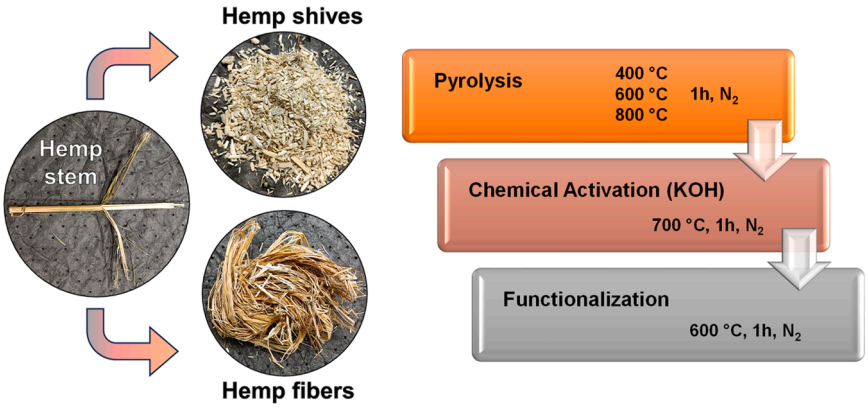

Fig. 1. Hemp stem-derived substrates, shives and fibers, were used to synthesize electrocatalysts for oxygen reduction reaction (ORR) through three main processes: 1) pyrolysis at three different temperatures (400, 600 and 800 °C); 2) chemical activation with KOH as reagent; and 3) functionalization, with iron phthalocyanine (FePc) as a precursor.

Jobin Yvon, France) to collect the signals. The two main Raman peaks remained the D and G bands: the G-band (ca. 1575 cm^{-1}) relates to graphitic (sp^2) carbon, while the d-band (ca. 1320 cm^{-1}) emerges due to discontinuities, disorder, and sp^3 hybridizatized carbon species. To determine the I_D/I_G ratio, as a matrix to estimate defect density, the normalized intensities of the D and G bands were estimated, typically as the height from the baseline to the peak maxima. The I_D/I_G ratios were then calculated by dividing the intensity of the d-peak by that of the G-peak.

For morphological examination, scanning electron microscopy (SEM) images of the synthesized carbonaceous electrocatalysts were captured using a FEI Helios Nanolab 650 instrument (Hillsboro, OR, USA).

The porosity of the samples was assessed with ^{129}Xe NMR, following a previously reported procedure [35]. About 0.1–0.15 g of carbon powder was inserted in NMR glass tubes (10 and 8 mm of outer and inner diameter, respectively). The tubes were degassed by a dynamic vacuum with a Schlenk line. Then, tubes were filled with enriched xenon gas (isotopic enrichment of 86.6 % in the ^{129}Xe isotope). The gas was trapped inside the tubes by freezing with liquid nitrogen, and the tubes were flame sealed. The final nominal xenon pressure inside the tubes was in the range of 2.5–3 bar. ^{129}Xe NMR spectra were acquired on a Bruker Avance 500 spectrometer operating at a Larmor frequency of 500.13 MHz for ^{1}H (corresponding to 139.09 MHz for ^{129}Xe), equipped with a 10 mm direct broadband observe (BBO) probe. The free xenon gas peak was set at 0 ppm and used as an internal chemical shift reference. Spectra were acquired with a relaxation delay of 15 s and several scans in the range of 1024–4096 to ensure a good signal-to-noise ratio. Measurements were performed at different temperatures (298, 278, 258 and 238 K) by connecting a liquid nitrogen evaporator to the NMR probe. The evaporator and the temperature were controlled with a Bruker BVT3000 variable temperature unit with an uncertainty of 0.1 K.

The porosity of the samples was additionally evaluated by nitrogen adsorption porosimetry measurements that were carried out at 77 K with a TriStar II PLUS system (Micromeritics) after a drying step for 24 h at 413 K under N_2. The N_2 adsorption isotherms were analyzed by the Brunauer-Emmett-Teller (BET) and density functional (DFT) theories to obtain the specific surface area (S_{BET}) and pores size distribution (PSD), respectively.

Transmission Electron Microscopy (TEM) and Scanning Transmission Electron Microscopy (STEM) was adopted to define the presence and the nature of nanoparticles at the various explored temperatures. A Talos F200X G2 TEM microscope was used for such characterization, using a beam energy of 200 keV.

2.2.2. Chemical characterization

A first attempt to qualitatively determine the elemental composition of the synthesized electrocatalysts was performed with Energy-dispersive X-ray fluorescence (XRF), which had an X-ray tube with a molybdenum anode (Bruker Artax 200 spectrometer). Elemental composition was further investigated with the FEI-SEM microscope (Helios Nanolab 650) equipped with an energy-dispersive X-ray spectrometer (EDX, X-Max Oxford).

The surface chemistry of all samples was quantitatively analyzed using X-ray photoelectron spectroscopy (XPS) with a Nexsa spectrometer (England), which was equipped with a monochromatic, micro-focused Al Kα X-ray source (photon energy 1486.6 eV). Survey and high-resolution spectra were collected at pass energies of 200 eV and 50 eV, respectively, with the source operating at a typical power of 72 W. The binding energies of all elements were recalibrated by setting the C—C/C—H component of the adventitious carbon first peak at 285 eV. Measurements were performed under ultra-high vacuum (UHV) conditions, with a base pressure of 5×10^{-10} torr, not exceeding 3×10^{-9} torr.

2.3. Electrochemical characterization of the electrocatalysts

For the electrochemical analysis, the ink was prepared by suspending 5 mg of the synthesized electrocatalyst in a solution consisting of 985 μL isopropanol (Alfa Aesar) and 15 μL of 5 wt % Nafion®d-520 (Alfa Aesar). This mixture was then subjected to probe sonication for 10 min followed by bath sonication for 30 min, both at room temperature. After achieving a homogeneous ink, two different electrocatalyst loadings (0.2 mg cm^{-2} and 0.6 mg cm^{-2}) were used to fabricate the working electrode on an E6R2 series rotating ring disk electrode (RRDE) [36].

Experiments were conducted in a three-electrode configuration, with a graphite rod as the counter electrode, RRDE as the working electrode and a saturated calomel electrode (SCE) as the reference electrode, with the electrolyte being O_2-saturated 0.1 M KOH solution. To record the electrochemical response, Pine Wave Vortex RDE setup connected to a Pine bipotentiostat was used, while 85 % IR compensations were applied with an SP-100 Biologic®. All potentials in this study were referenced to the reversible hydrogen electrode (RHE) by adding a factor of '0.241 + [pH] x 0.0591' to the measured potentials (referenced to SCE).

Linear sweep voltammetry (LSV) was performed to obtain polarization curves at a scan rate of 5 mV s^{-1} between 1200 and 0 mV vs. RHE, with the ring potential held at ~1200 mV vs. RHE and the RRDE rotating at 1600 rpm. Prior to recording the actual LSV curves, the electrocatalyst was conditioned through multiple cyclic voltammograms until a stable current was achieved. Both the disk current (I_{disk}) and ring current (I_{ring}) of the RRDE were recorded over the whole potential window. The onset potential (E_{onset}) and half-wave potential ($E_{1/2}$) were derived from the

I_{disk}, serving as kinetic indicators to compare the electroactivity of the different synthesized electrocatalysts. E_{onset}, which indicates the threshold potential to initiate the ORR, was determined at −0.1 mA cm^{-2}. $E_{1/2}$ was identified at the peak of the first derivative of the LSV, following established ORR protocols. Additionally, the peroxide anion yield (%) and the number of transferred electrons (n) during the ORR were estimated using Eq. (1) and Eq. (2), respectively. These parameters are required to assess the reaction's selectivity towards the 4-electron pathway, minimizing the production of peroxide anions in the alkaline media.

$$\text{Peroxide anion yield}\left(HO_2^-,\ \%\right) = \frac{200 \times \frac{I_{ring}}{N}}{I_{disk} + \frac{I_{ring}}{N}} \quad \text{(Eq. 1)}$$

$$n = \frac{4 \times I_{disk}}{I_{disk} + \frac{I_{ring}}{N}} \quad \text{(Eq. 2)}$$

The electrochemical stability of one of the electrocatalysts derived from hemp fibers (HF 600) was also assessed by applying 2000 cycles at a scan rate of 50 mV s^{-1} in the O_2-saturated 1 M KOH electrolyte, with the rotating disk electrode (RDE) at a speed of 1600 rpm and an electrocatalyst loading of 0.6 mg cm^{-2}. For comparison, ORR polarization curves were obtained again at a scan rate of 5 mV s^{-1} after the 2000 cycles. The stability test was carried out in the potential window of 1.1–0.3 V vs RHE.

3. Results and discussion

3.1. Synthesis of the electrocatalysts

The synthesis process of the electrocatalysts was successfully done for three different pyrolysis temperatures (400, 600 and 800 °C) and two different substrates (hemp shives and hemp fibers). For hemp shives (HS), the pyrolysis yields were 33.5, 27.7 and 26.0 % at each temperature, respectively, while for hemp fibers (HF) yields were slightly lower, i.e. 29.7, 22.6 and 23.2 %, respectively. The chemical activation rates mainly varied depending on the type of substrate, being 47.2, 54.7 and 57.5 % for HSs pyrolyzed at 400, 600 and 800 °C, respectively, and 20.1, 29.4 and 20.5 % for HFs undergoing the same heat treatment, respectively. The sample yield during the activation process could also be affected by the handling and washing during the activation procedure.

3.2. Structural properties of the electrocatalysts

XRD patterns for hemp shives (HS) and fibers (HF) derived electrocatalysts are displayed in Fig. 2a and Fig. 2b, respectively. Every sample shows two broad peaks at around 24° and 42°, which are attributed to the crystallographic planes (002) and (101) of graphite (ICDD: 01–089–7213), respectively, indicating the defective nature of the graphitic matrix. A few tiny peaks are identified at ca. 35.7°, 57° and 62°, which can associated with iron oxide in the form of magnetite (ICDD: 01–075–0449). This goes in accordance with the presence of iron in the amorphous carbon matrix, as determined by a wide variety of semi-quantitative and quantitative characterization techniques (see Section 3.4). A minor peak at ca. 27° can be attributed to SiO_2 (ICDD: 01–089–8941) and may originate from the XRD sample holder.

To study the carbon structure of the electrocatalysts, Raman spectroscopy was employed; see recorded spectra in Fig. 3a and Fig. 3b for HS and HF derived electrocatalysts, respectively. The spectra are mainly composed of two broader peaks in the vicinities of 1575 cm^{-1} and 1320 cm^{-1} that can be attributed to the G and D bands, respectively. The G band is the characteristic band of the graphitic material and is linked with the bond stretching of all pairs of sp^2 carbon atoms in both rings and chains, whereas the D band appears due to the breathing of sp^2 atoms in rings and indicates the presence of structural defects and discontinuities in the carbon. The intensity ratio of the D to G band (I_D/I_G) is a typical parameter to estimate the defect density, see Fig. 3a and Fig. 3b Quite interestingly, the overall defect densities in the hemp fibers derived electrocatalysts are higher compared to the ones derived from shives. Samples HS400 and HF400, acquired at the lowest first pyrolysis temperature (400 °C), have comparable intensities of D and G bands and, therefore, the I_D/I_G ratios are relatively lower (ca. 1.1) compared to the other counterparts. However, the corresponding values increase as the temperature increases. HS600 and HF600 exhibit I_D/I_G ratios of ca. 1.5, meaning a highly defect-rich structure that could favor ORR due to structural discontinuities like broken edges and defective graphitic domains, which help in the binding of oxygen.

3.3. Morphology of the electrocatalysts

SEM images are used to analyze the morphological characteristics of the electrocatalysts, including particle size, distribution, shape, surface roughness, and porosity. Fig. 4 displays backscatter images of all six synthesized electrocatalysts at a magnification of 2500x with a 20 μm scale bar (see Figure S1 for similar images at 1000x magnification). Each sample exhibits particles ranging in size from approximately 5 to 50 μm, indicating minimal mechanical disruption of the particles. Notably, electrocatalysts derived from hemp fibers tend to have slightly larger particles compared to those from hemp shives.

Regarding particle shape, those pyrolyzed at 400 °C exhibit a more rounded morphology, forming rough spheres. In contrast, those pyrolyzed at 600 and 800 °C for both substrate types display a more

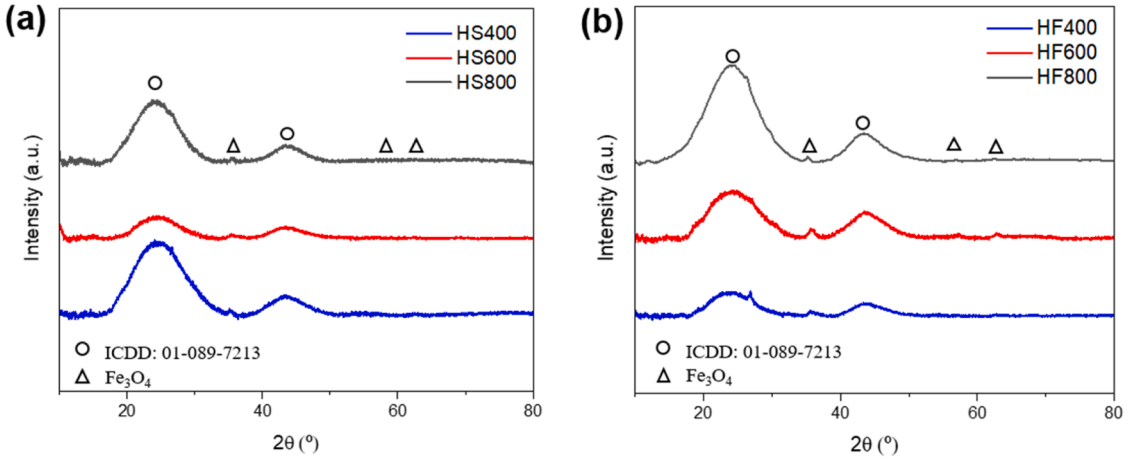

Fig. 2. XRD patterns of (a) HS and (b) HF derived electrocatalysts.

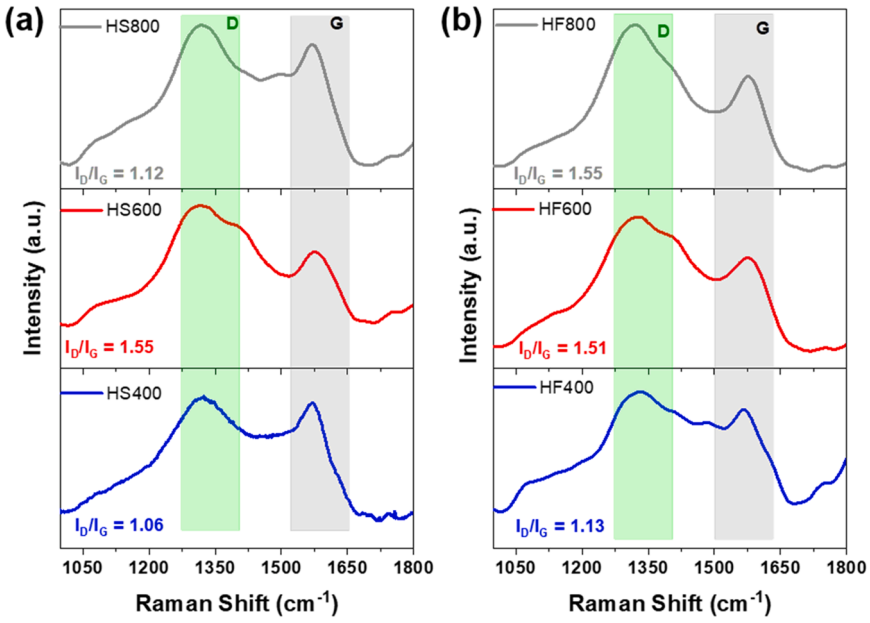

Fig. 3. Raman Spectra of (a) HS and (b) HF derived electrocatalysts.

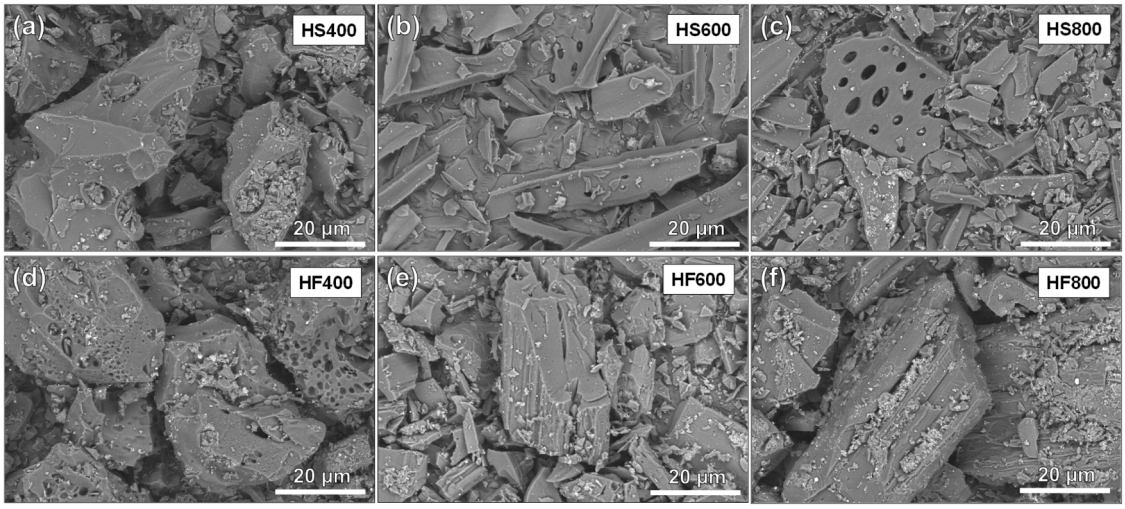

Fig. 4. Backscattered SEM images at a magnification of 2500x for (a-c) HS and (d-e) HF derived electrocatalysts. Dwell time: 30 µs.

elongated polyhedral shape. SEM images reveal visible surface irregularity and porosity in every carbonaceous electrocatalyst, suggesting increased roughness and additional pore formation after activation. Rounded particles show multiple cavities and large surface pores, whereas elongated particles exhibit polygonal faces, straight edges, sharp vertices, and elongated pores visible in cross-sections. SEM images from previous work [37] have shown that hemp shives have a unique connected and hierarchical pore geometry already visible in the raw material.

To further investigate the variation of the porosity of the samples along with the different treatment, ^{129}Xe NMR measurements were conducted [38,39]. To recollect, the different steps of the electrocatalyst preparation were: i) first pyrolysis (transformation of HS or HF into conductive char), ii) activation process that include treatment with KOH and pyrolytic process, iii) functionalization of the conductive activated char with FePc.

^{129}Xe NMR spectra of hemp shives (HS) and hemps fibers (HF) subjected to first pyrolysis at 400 °C show the intense and sharp free xenon gas peak, set to 0 ppm and used as an internal chemical shift reference, along with a broad and very weak resonance centered roughly in the range between 170 ppm and 180 ppm (Figure S2). This peak derives from xenon sorbed into the porous structure of the pyrolyzed materials [39]. Its low relative intensity indicates that the porosity of these materials is overall very low. For the HF pyrolyzed at 600 °C, the spectra show that these materials do not have any significant porous structure in the dimensional range probed by xenon NMR, similarly to the fibers pyrolyzed at 400 °C (Figure S3). On the other hand, HS have a different morphology compared to those pyrolyzed at 400 °C. In the room temperature spectrum (278 K), the intense peak centered at roughly 175 ppm reveals the presence of a porous structure generated by the thermal treatment. By lowering the temperature to 258 K, and especially 238 K, the peak splits into two broad resonances. This indicates that the sample has two different populations of pores which become distinguishable only when the xenon dynamics is slowed down by the low temperature. At 278 K and higher, xenon atoms exchange rapidly between the two different populations, and this results in a single average NMR signal. Based on the chemical shifts of the peaks, which are 170 ppm and 221 ppm, respectively, these signals can be qualitatively attributed to

micropores with different sizes [40]. In addition to that, the free gas peaks in the spectra of hemp shives have shoulder peaks similar to those visible in Figure S2. This indicates that the large macroporous spaces are retained even when the first pyrolysis is performed at 600 °C. Interestingly, the morphology of the HS and HF is completely changed when the pyrolysis is performed at 800 °C (Figure S4). In fact, ^{129}Xe NMR spectrum of pyrolyzed HF acquired at 298 K displays two partially superimposed peaks that suggest the presence of two different populations of pores. The presence of a bimodal porous structure is confirmed by low-temperature measurements in which the separation between the peaks is increased along with their intensities relative to the free gas peak. On the other hand, the HS subject to the first pyrolysis at 800 °C do not show any significant micro- and mesopores (dimensions between 2 nm and 50 nm), similar to the HF pyrolyzed at 400 °C and 600 °C. Only large macroporous indentations are visible at 258 K and 238 K, analogous to the lower pyrolysis temperatures. These results indicate that either the high processing temperature breaks down the pores, increasing their sizes to the point where xenon in the middle of the pores cannot be distinguished from the free xenon gas (i.e. big macropores such as those visible in the SEM images in Fig. 4), or that the small pores are obstructed by ashes or other residues formed during the first pyrolysis.

The effect of the activation with KOH on the carbon morphology was studied by analyzing some of the activated samples with ^{129}Xe NMR and comparing the spectra with those of the corresponding materials after first pyrolysis. In the case of the HF treated at 400 °C, the activation procedure generates a bimodal porous structure in the pyrolyzed HF (Figure S5). Variable temperature spectra demonstrate that there is a significant segregation between the two different populations of pores, as even at room temperature xenon gas is not able to exchange rapidly between them on the NMR time scale. The activation with KOH generates a different porous structure in the HF treated at 600 °C (Figure S6). Here, the spectrum at 298 K shows a single resonance with a chemical shift of 97 ppm, thus, the activation process generates a rather homogeneous porous structure with a monomodal distribution of pores estimated to be roughly in the mesopore range based on the chemical shift [39]. Interestingly, a similar morphology is obtained after the activation of HSs pyrolyzed at 600 °C (Figure S7), even though the porous structure of the starting material is completely different from that of the HFs (see Figure S3). The activation with KOH breaks down the bimodal porous structure of the HS, generating a single population of mesopores with rather homogeneous sizes.

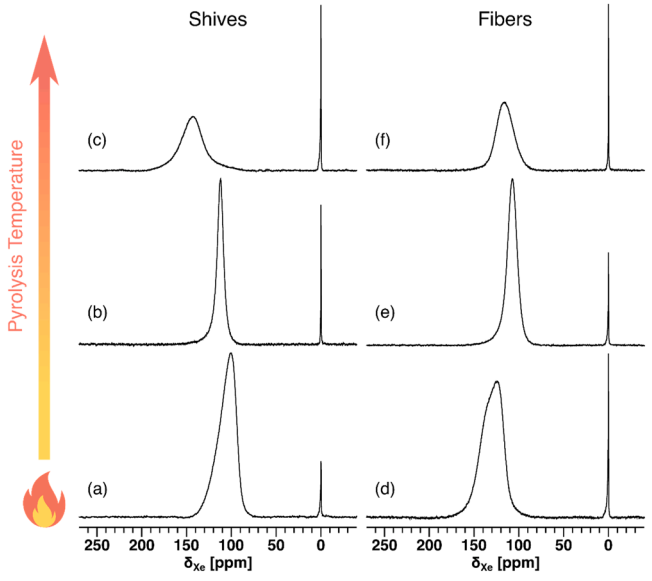

Fig. 5. ^{129}Xe NMR spectra acquired at 278 K (5 °C) of HS (a, b, c) and HF (d, e, f) derived electrocatalysts pyrolyzed at 400, 600 and 800 °C, respectively.

^{129}Xe NMR spectra recorded at 278 K are presented in Fig. 5 for all electrocatalysts prepared by functionalizing the activated materials with FePc, which represent the last step of the synthetic process. Single downfield peaks are evident in each spectrum, indicating that all the electrocatalysts possess a notable porous structure in the dimensional range detectable by xenon. For all samples, the pore sizes can be qualitatively estimated to fall within the mesopore range, based on the chemical shifts of the peaks, between 100–150 ppm [39]. The broadness of the peaks in Fig. 5a, d and Fig. 5c, f reveals that the electrocatalysts obtained when the starting materials are pyrolyzed at 400 °C, and especially at 800 °C, have a heterogeneous morphology characterized by interconnected pores with different dimensions. Additionally, the downfield peaks in the spectra of samples pyrolyzed at 400 °C are asymmetric and skewed toward higher chemical shifts, denoting that, among the heterogenous pore structure, there is a significant number of small pores that fall into the small meso- or micropore range (Fig. 5a, d).

In contrast, the peaks from the electrocatalysts obtained after the pyrolysis at 600 °C are sharper and only slightly asymmetric at the base (Fig. 5b, e), suggesting that they have the most uniform porous structures along the series, similar to what was observed for the activation process. Interestingly, these materials also showed the best electrocatalytic performance for the oxygen reduction reaction (see below) [41]. However, the relatively narrow linewidth of the xenon resonances indicates the presence of isolated iron atoms and non-metallic nanoparticles, since for this last case, xenon linewidth would be hundreds of ppm [41]. The relatively narrow linewidth of the xenon resonances suggests that iron is present as isolated atoms rather than in the form of metallic nanoparticles. Iron-based nanoparticles typically create significant inhomogeneities in the local magnetic field, which dramatically shorten the T2 relaxation time—this property is the reason why such particles can be used as MRI contrast agents [42]. Low relaxation times would produce linewidths of tens or hundreds of ppm, as seen for example in rocks containing magnetite [43].

Anyways, these results indicate that a homogeneous porous structure is a favorable factor for the performance of the hemp-derived electrocatalysts. The morphological uniformity likely enhances the mass transport and the accessibility of the electrocatalytic sites to the reactants and guarantees that the active sites are well distributed inside the electrocatalyst, leading to improved efficiency. By contrast, the heterogeneous porous structures of the other materials may hinder the ORR, resulting in worse electrocatalytic activities, especially in terms of peroxide production and number of transferred electrons. For all the samples, no significant variations of the peak shapes and no additional peaks are observed upon lowering the temperature (Figure S7).

The evolution of the morphology of the material is exemplified in Fig. 6 for the fibers treated at 400 °C. If the pyrolyzed fibers present just a broad and very weak peak centered at 170 ppm, the spectrum of the activated material shows an intense peak at 127 ppm and a smaller downfield peak at 150 ppm which are related to a bimodal porous structure with significant segregation between the two pore populations. In the spectrum of the electrocatalyst, the width of the peaks is significantly higher, and the smaller downfield peak is partially superimposed to the more intense central peak. This indicates that functionalization increases the pore heterogeneity and decreases the segregation between the two pore populations. This effectively transforms the bimodal porous structure of the activated material into a heterogeneous distribution of mesopores in the electrocatalyst in which xenon atoms are able to exchange through all the different spaces during the NMR experiment.

The evaluation of the textural properties was carried out by analyzing the N_2 adsorption/desorption isotherms at 77 K that are reported in Fig. 7. At low pressures, the isotherm branches of all the analyzed samples illustrated sharp adsorption inflections which are indicative of materials containing micropores. In the case of carbons derived from HS, adsorption at the lowest relative pressure decreases in the order 600 °C > 400 °C > 800 °C, suggesting a parallel decrease of

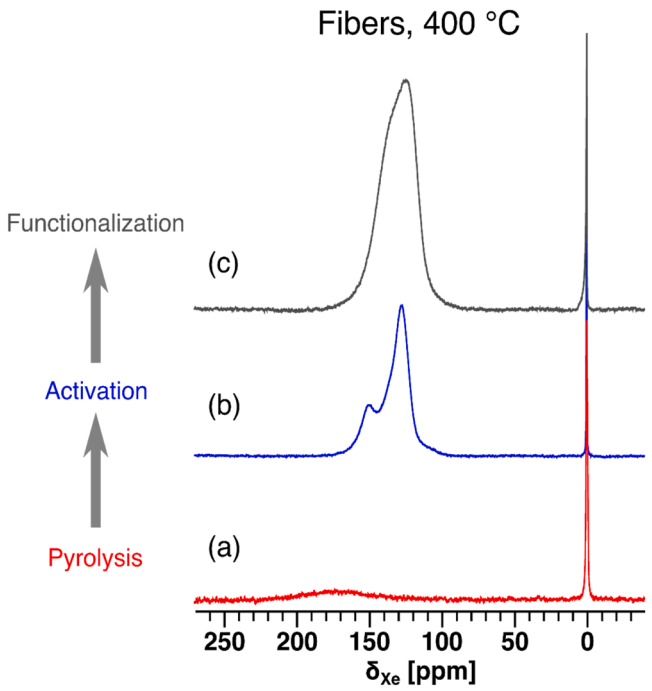

Fig. 6. ^{129}Xe NMR spectra of hemp fibers (a) after pyrolysis at 400 °C, (b) after activation with KOH, and (c) after functionalization with FePc. The spectra were acquired at 278 K.

microporosity (Fig. 7a). In the case of carbons derived from HF, the adsorption at the lowest relative pressure decreases with the decrease of the pyrolysis temperature in the order 800 °*C* > 600 °*C* > 400 °C. Thus, an increase in microporosity is observed with the increase in the treatment temperature. In addition, at higher relative pressures ($P/P_0 > 0.4$), the carbon derived from the treatment of HF at 800 °C (Fig. 7b) displayed type IV isotherm adsorption-desorption branches showing the existence of mesopores. On the other hand, all the other samples featured a type I isotherm that describes microporous materials [44].

These observations are confirmed by the DFT pore size distribution that is reported in terms of incremental pore volume in Fig. 7c-d. In the case of carbons derived from hemp shives (Fig. 7c), the majority of the pore volume is given by micropores < 2 nm. Notably, the pore volume given by micropores decreases in the order 600 °C (0.574 $cm^3\ g^{-1}$) > 400 °C (0.534 $cm^3\ g^{-1}$) > 800 °C (0.391 $cm^3\ g^{-1}$). In addition, all three samples derived from hemp shives feature a small quantity of mesopores at > 10 nm. For the samples treated at 600 °C and 800 °C, there is a small increase in the pore volume given by mesopores (0.020 $cm^3\ g^{-1}$ vs. 0.011 $cm^3\ g^{-1}$).

A similar behavior was observed for the carbons derived from hemp fibers (Fig. 7d), in which the majority of the pore volume is given by micropores < 2 nm. In particular, the microporosity of the carbons increases as the temperature increases, with pore volumes given by micropores of 0.470 $cm^3\ g^{-1}$, 0.618 $cm^3\ g^{-1}$, and 0.647 $cm^3\ g^{-1}$ for HF 400, HF 600, and HF 800, respectively. For the carbon obtained with the pyrolysis at 800 °C, there are more mesopores (especially between 2 and 4 nm) with respect to the other two samples, with an almost double V_{meso} (0.060 $cm^3\ g^{-1}$).

The micropore volume (V_{micro}), mesopore volume (V_{meso}) and total pore volume (V_{total}) of the different samples are summarized in Table 1 along with the BET surface area (S_{BET}).

The S_{BET} decrease is consistent with the decrease of the micropore and mesopore volume. Indeed, for the HS derived electrolcatalysts, the BET surface area decreases in the order 600 °C (1494.5 $m^2\ g^{-1}$) > 400 °C (1436.4 $m^2\ g^{-1}$) > 800 °C (1074.7 $m^2\ g^{-1}$). In the case of HF derived electrocatalysts, the BET surface area decreases in the order 800 °C (1735.6 $m^2\ g^{-1}$) > 600 °C (1637.7 $m^2\ g^{-1}$) > 400 °C (1228.8 $m^2\ g^{-1}$).

In summary, in the case of carbons derived from HF, microporosity, mesoporosity, and BET surface area increase with the increase of the pyrolysis temperature. On the other hand, in the case of carbons derived from HS, microporosity and BET surface area increase in the order 800 °*C* then 400 °*C* and finally 600 °C; while mesoporosity increases from ≥ 600 °C as pyrolysis temperature.

3.4. *Surface chemistry of the electrocatalysts*

The first approach to evaluate the elemental composition of the synthesized electrocatalysts was done with XRF, showing that iron is the only metal present in all the samples (see Figure S8). This iron content is related to the FePc precursor used to functionalize samples. As a confirmation, SEM energy dispersive X-Ray (EDX) maps were acquired to determine the distribution of iron compounds. Figure S9 shows that samples consisted of C, O and Fe homogeneously distributed throughout the whole carbonaceous structure, with little formation of iron clusters. Overall, it appears that iron content is larger in HF than in HS derived samples. Nitrogen could be detected as a minor constituent. This proves that the mixing of the FePc precursor with the activated carbon powder, as well as the further heat treatment, properly functionalizes the electrocatalysts.

Bright Field (BF) STEM images highlight the presence of nanoparticles in all electrocatalysts, despite the heat treatment. Fig. 8 collects STEM images taken at a magnification of 750 kX, while in Figure S10 and Figure S11 STEM BF and TEM images can be seen at lower magnifications, 135 kX and 56 kX, respectively. An increase in particle size can be noticed inside the single series (HS or HF), which starts with a dispersion of particles of approximately 5–10 nm at 400 °C, ending with a bigger dimensional dispersion at 800 °C, with fewer small particles and the appearance of fewer big particles. Fast Fourier Transform on the HR-TEM images shows the presence of Fe_3O_4 (magnetite) main d-spacings for all the samples. No metallic Fe is visible (Si information and Figure S12).

The surface chemistry of all electrocatalysts was thoroughly analyzed using XPS. The acquired survey scans are demonstrated in Figure S12, which confirm the presence of the elements of interest, i.e. C, N and Fe, whereas their relative proportions are summarized in Table S1. Overall, HF derived electrocatalysts demonstrate relatively higher amounts of nitrogen and iron than HS derived ones, as deduced from EDX spectra. Interestingly, as the pyrolysis temperature increases, the relative nitrogen and iron content tends to slightly decrease. The Fe 2p high-resolution spectra provided in Figure S13 indicate the occurrence of both Fe^{+2} and Fe^{+3} type species in the samples.

It is important to underline that nitrogen is the key ingredient of the M-N-C structures, since it breaks the carbon's electroneutrality and gives rise to various active moieties that uniquely take part in the ORR [45, 46]. By deconvoluting the N 1 s spectra, various nitrogen-based moieties such as pyridinic, metal coordinated with nitrogen (N_x-Me), pyrrolic, graphitic and quaternary nitrogen can be detected, as shown in Fig. 9. They are identified through deconvoluted peaks assigned to specific binding energies, as extensively discussed in the literature [46–48].

Each active moiety plays a particular role in ORR, and the overall ORR is the collective response of all the present moieties. For instance, the key active sites for ORR are the atomically dispersed and easily accessible N_x-Me, since they carry out ORR in the four-electron fashion with complete reduction of oxygen into water or OH^- in the acidic or alkaline media, respectively [48,49]. On the other hand, pyrrolic nitrogen is known for the two-electron ORR, giving undesired peroxide as the final product. Meanwhile, pyridinic nitrogen is capable of stepwise completing the ORR by further reducing the produced peroxide and is, therefore, regarded as the second most important active site [47].

As for graphitic nitrogen, it not only increases the peroxide yield but also affects the E_{onset} and $E_{1/2}$ potentials [50]. Quaternary-N has a similar structure as the graphitic-N; however, the nitrogen contains *a* +

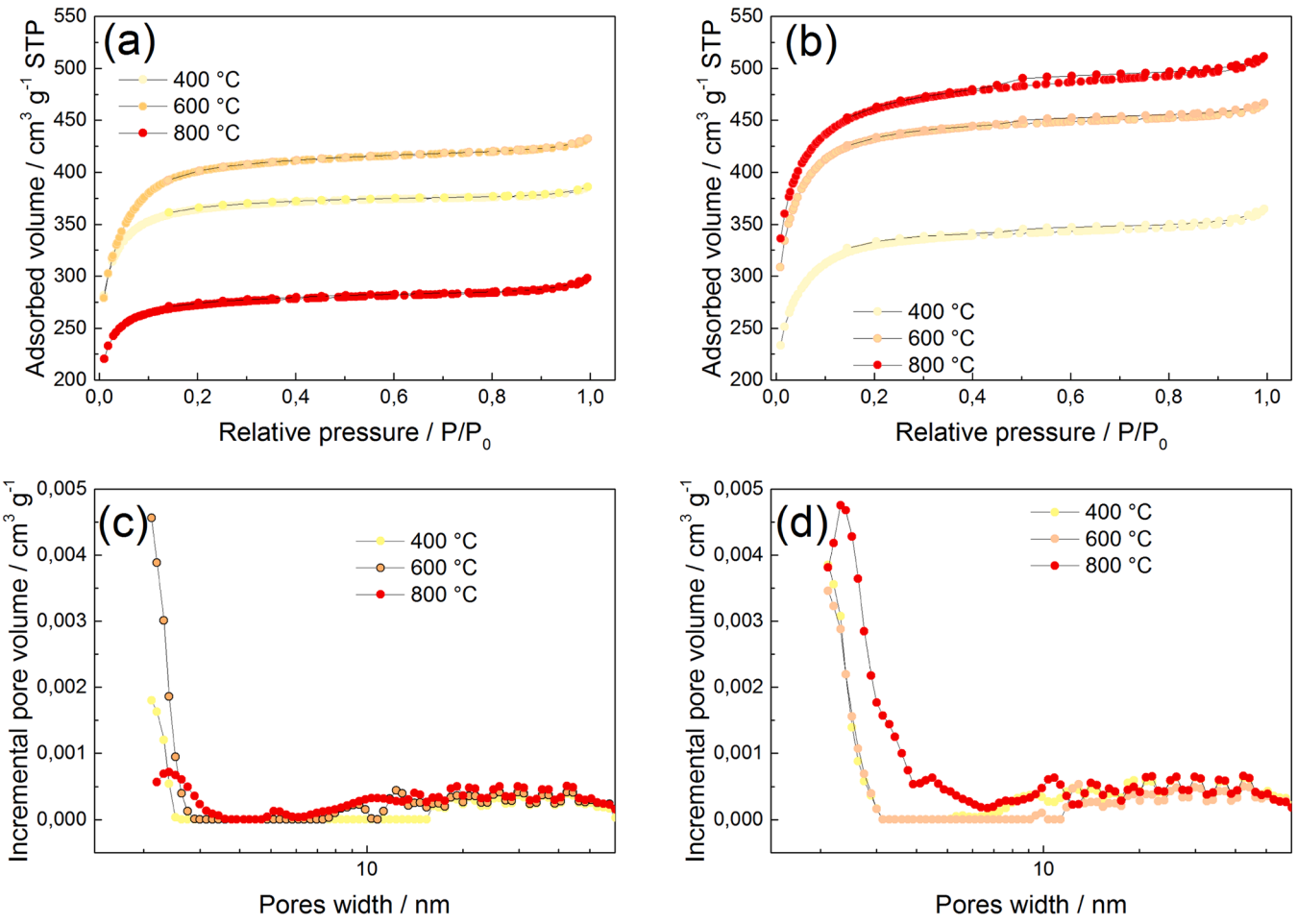

Fig. 7. N_2 adsorption/desorption isotherms of the produced carbon materials from a) electrocatalysts from hemp shives, HS, and b) electrocatalysts from hemp fibers, HF. Pore size distribution of c) electrocatalyst from HS, and d) electrocatalyst from HF.

Table 1
DFT micropore volume (V_{micro}), mesopore volume (V_{meso}) and total pore volume (V_{total}) and BET-specific surface area (S_{BET}), of the different samples.

Samples	V_{micro} (< 2 nm) $cm^3\ g^{-1}$	V_{meso} (2 −50 nm) $cm^3\ g^{-1}$	V_{total} $cm^3\ g^{-1}$	S_{BET} $m^2\ g^{-1}$
HS 400	0.534	0.011	0.547 (< 99.9 nm)	1436.4 ± 1.7
HS 600	0.574	0.022	0.599 (< 99.9 nm)	1494.5 ± 13.4
HS 800	0.391	0.020	0.415 (< 99.9 nm)	1074.7 ± 2.4
HF 400	0.470	0.032	0.506 (< 99.9 nm)	1228.8 ± 9
HF 600	0.618	0.024	0.646 (< 99.9 nm)	1637.7 ± 11.7
HF 800	0.647	0.060	0.712 (< 99.9 nm)	1735.6 ± 10.2

1 charge [47]. It should be noted that the Nx-Me, specifically Fe-N_x in the case of Fe-N-C, are the key active sites that are not only important in carrying out a complete ORR but also help in reducing the peroxide anions in OH^- in the stepwise reaction pathway. The influence of the iron oxide i.e. Fe_3O_4 nanoparticles towards the ORR capability of Fe-N-C has also been reported in the literature [51,52]. Tylus et al. confirmed the active role of Fe-Nx type species in the alkaline ORR while they observed that iron-based nanoparticles can act as secondary sites 2e− × 2e− mechanism, particularly in acidic media [52]. On the other hand, Hu and coworkers witnessed the synergistic effect of Fe_3O_4 supported on Fe-N-C towards ORR in the alkaline media [51].

The relative distributions of different nitrogen-based moieties are presented in Fig. 10. The low-temperature pyrolyzed electrocatalysts, i.e. HS400 and HF400, have the maximum pyridinic nitrogen content, which gradually decreases with the increase in temperature. A similar trend is observed for the pyrrolic-N. On the contrary, electrocatalysts pyrolyzed at the highest temperature, i.e. 800 °C, have the highest graphitic nitrogen content. It should be noted that HF600 shows the maximum N_x-Me content together with the lowest graphitic-nitrogen level compared to other HF derived samples of the study. Moreover, the overall nitrogen and iron content of the HF derived samples is higher than the HS derived samples, as already shown in Table S1.

3.5. *Electrochemical activity of the electrocatalysts*

ORR measurements were carried out with the RRDE method in alkaline media with the aim of determining the electrocatalytic activity of the synthesized electrocatalysts in AEMFCs. Ink preparation resulted in a homogeneous mixture for every sample. All discussed data are supported by Table S2, which summarizes the main parameters, i.e. E_{onset} and $E_{1/2}$, describing the ORR performance of the synthesized electrocatalysts at loadings of 0.6 and 0.2 mg cm^{-2}.

Fig. 11 shows the electrochemical activity of HS derived electrocatalysts at a loading of 0.6 mg cm^{-2}, pyrolyzed at three different temperatures. The highest E_{onset} and $E_{1/2}$ values are achieved by HS600 with values of 0.96 and 0.92 V vs RHE, respectively. Although the J_{lmit} is maximum for HS800 (> 4.5 mA cm^{-2}), this sample has the highest

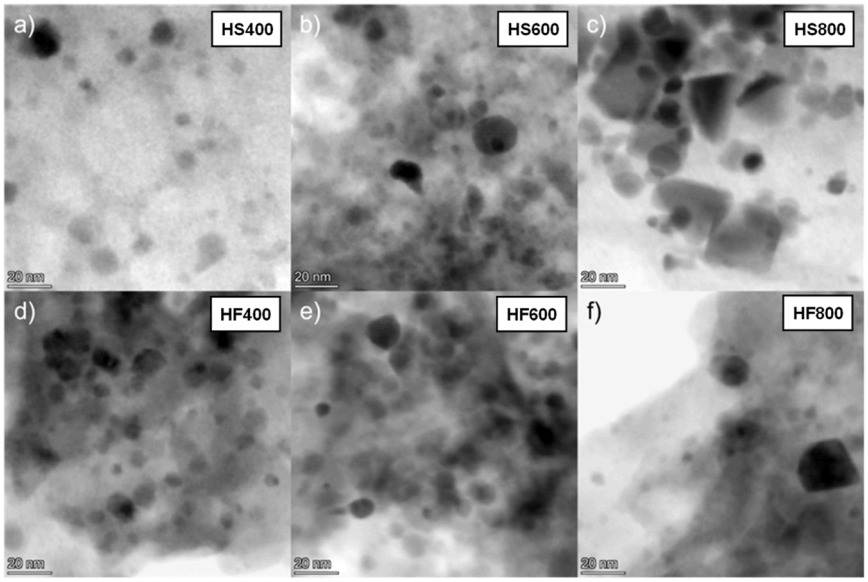

Fig. 8. STEM images at 750 kX of (a-c) HS and (d-f) HF derived electrocatalysts.

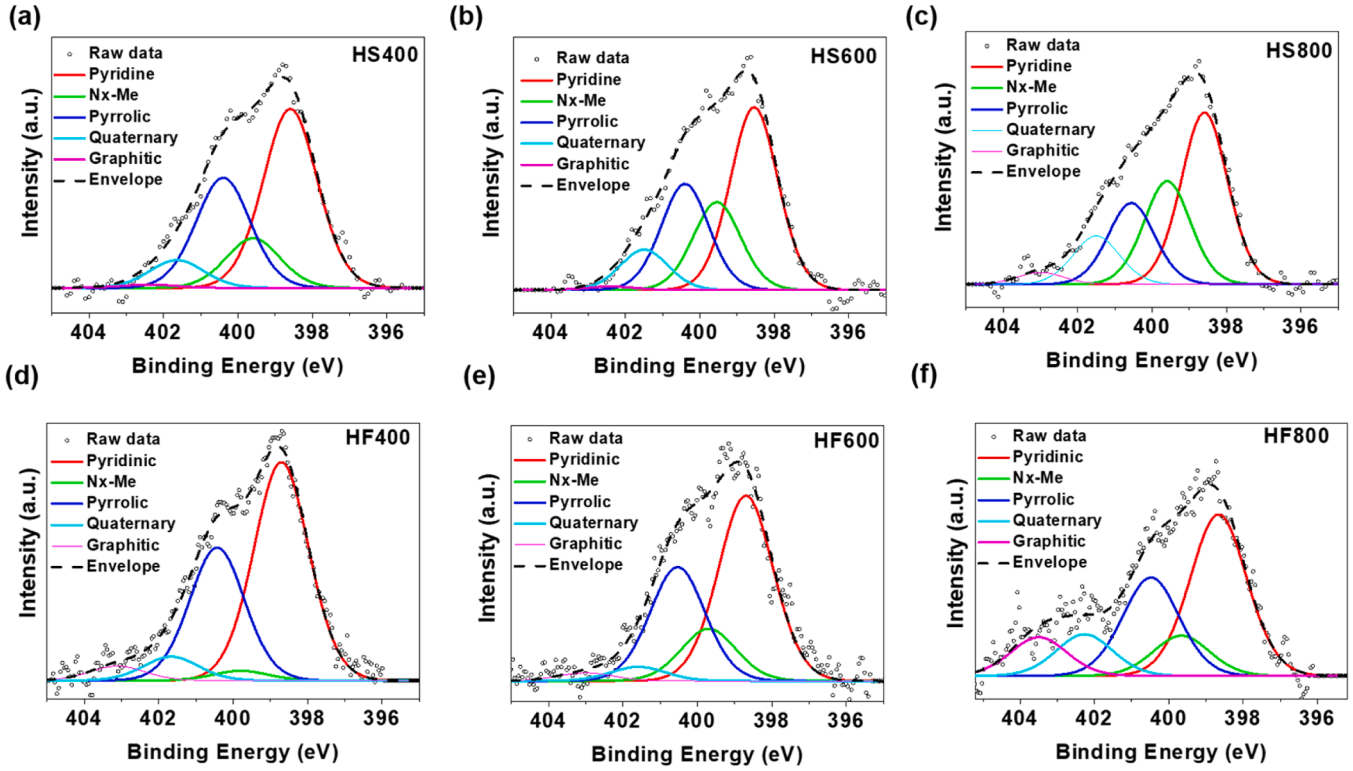

Fig. 9. High-resolution N 1 s XPS spectra of (a-c) HS and (d-f) HF derived electrocatalysts.

production of peroxide anion up to 17.5 % and the lowest electron transfer, which could relate to the higher content of graphitic and quaternary nitrogen as previously discussed. Interestingly, HS600 achieves the lowest peroxide anion yield (< 8 %) and the highest transferred number of electrons (n = 3.83). The observed J_{lmit} is slightly less than the theoretical value at 1600 rpm [53], apparently giving the impression that direct four-electron transfer which is preferable for fuel cells, may not be fully achieved [54]. This signifies the occurrence of diverse active sites, including those facilitating direct 4e$^-$ transfer, those enabling 2e$^-$ transfer, and others capable of further reducing intermediates to the final product and eventually creating a favorable situation[46].

Fig. 12 shows similar results for HF-derived electrocatalysts. In this case, again the highest E_{onset} and $E_{1/2}$ values are achieved by HF600, 0.97 and 0.92 V vs RHE, respectively. Looking at other parameters, this sample also obtains the highest I_{limit} (> 4 mA cm^{-2}) and the lowest peroxide anion production (< 7 %), with an electron transfer number of ca. 3.86. Figures S14 and Figure S15 illustrate the same performance parameters for the HS and HF-derived electrocatalysts, respectively, with a loading of 0.2 mg cm^{-2} in the RRDE. With a lower loading, the E_{onset} and $E_{1/2}$ values remain similar (see Table S2), but peroxide anion production is increased while the 4-electron pathway is less likely to occur, with a reduced limiting current too. The fact that higher loadings

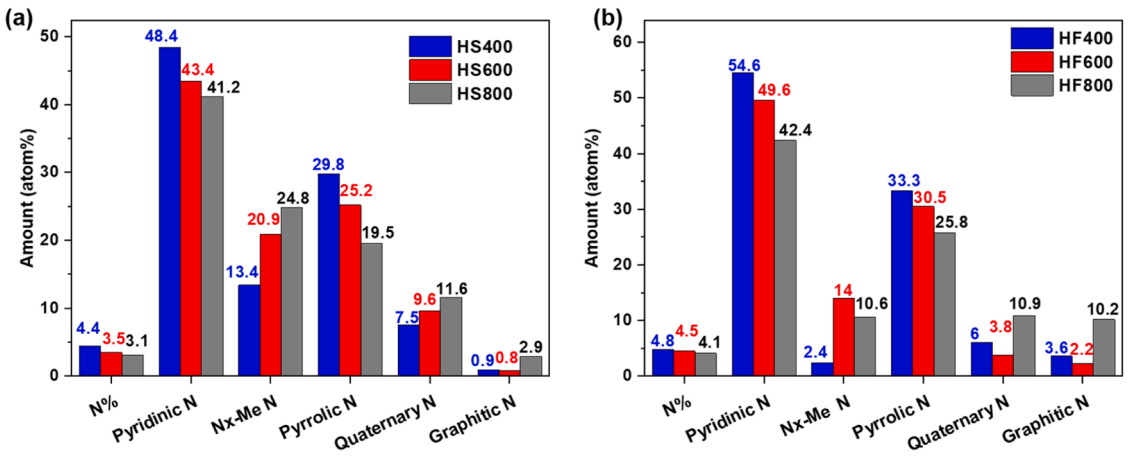

Fig. 10. Relative distribution of nitrogen content and different nitrogen-based moieties in the (a) HS and (b) HF derived electrocatalysts, estimated through the corresponding XPS N 1 s spectra.

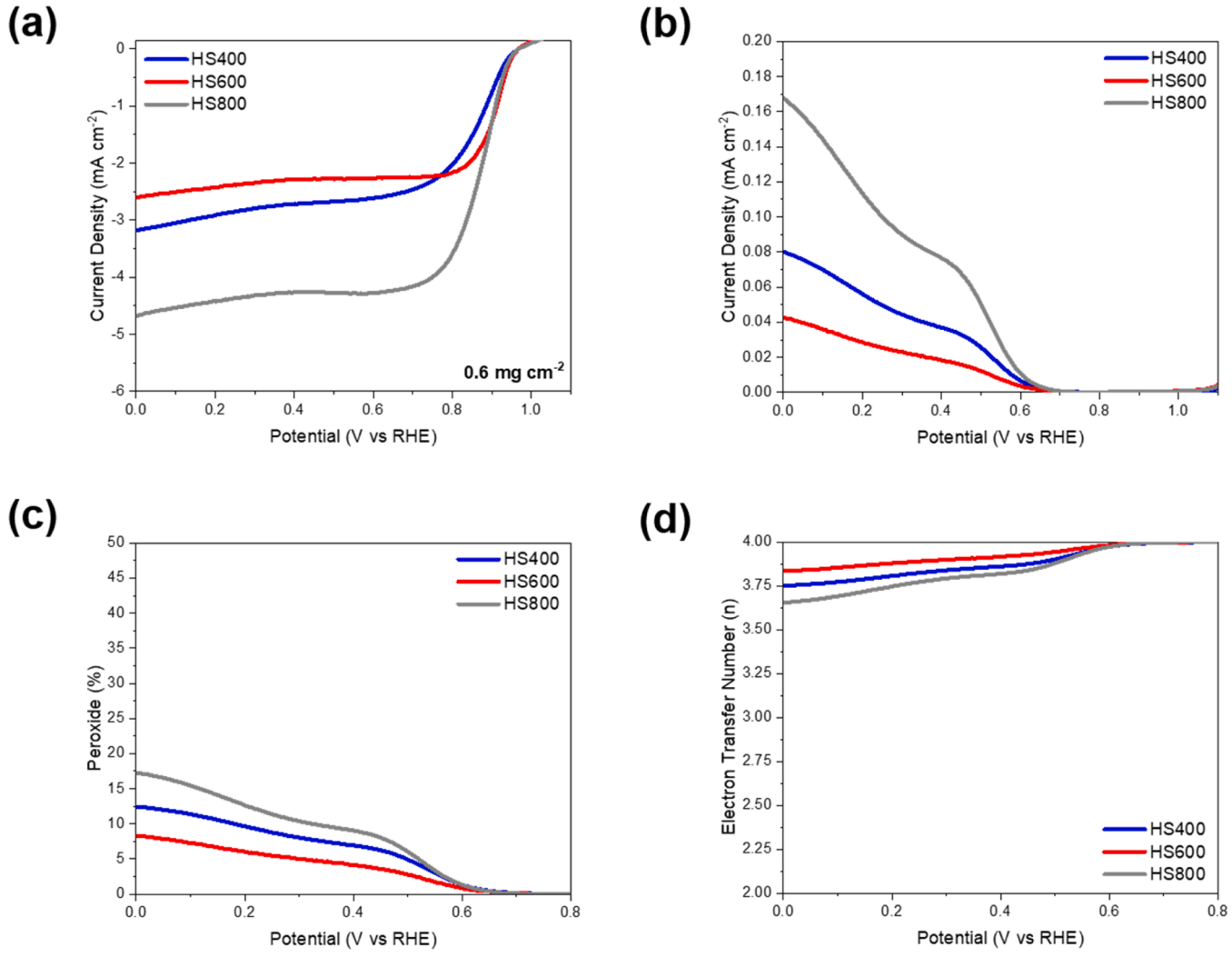

Fig. 11. RRDE measurements of the synthesized HS derived electrocatalysts in O_2-saturated 0.1 M KOH at 1600 rpm, with an electrocatalyst loading of 0.6 mg cm^{-2}. (a) LSV disk current densities at a scan rate of 5 mV s^{-1}, (b) ring current densities, (c) peroxide anion yield, and (d) the number of electrons transferred during ORR.

can scavenge peroxide production due to the denser electrocatalyst layer has already been reported in the literature [55,56] thereby these results fall within expectations.

The fact that both HS600 and HF600 achieved the highest E_{onset} and $E_{1/2}$, coupled with the lowest peroxide production among all the samples, seem to be closely related to the porous structure. In fact, these results indicate that a homogeneous porous structure is a favorable factor for the performance of hemp-derived electrocatalysts. The

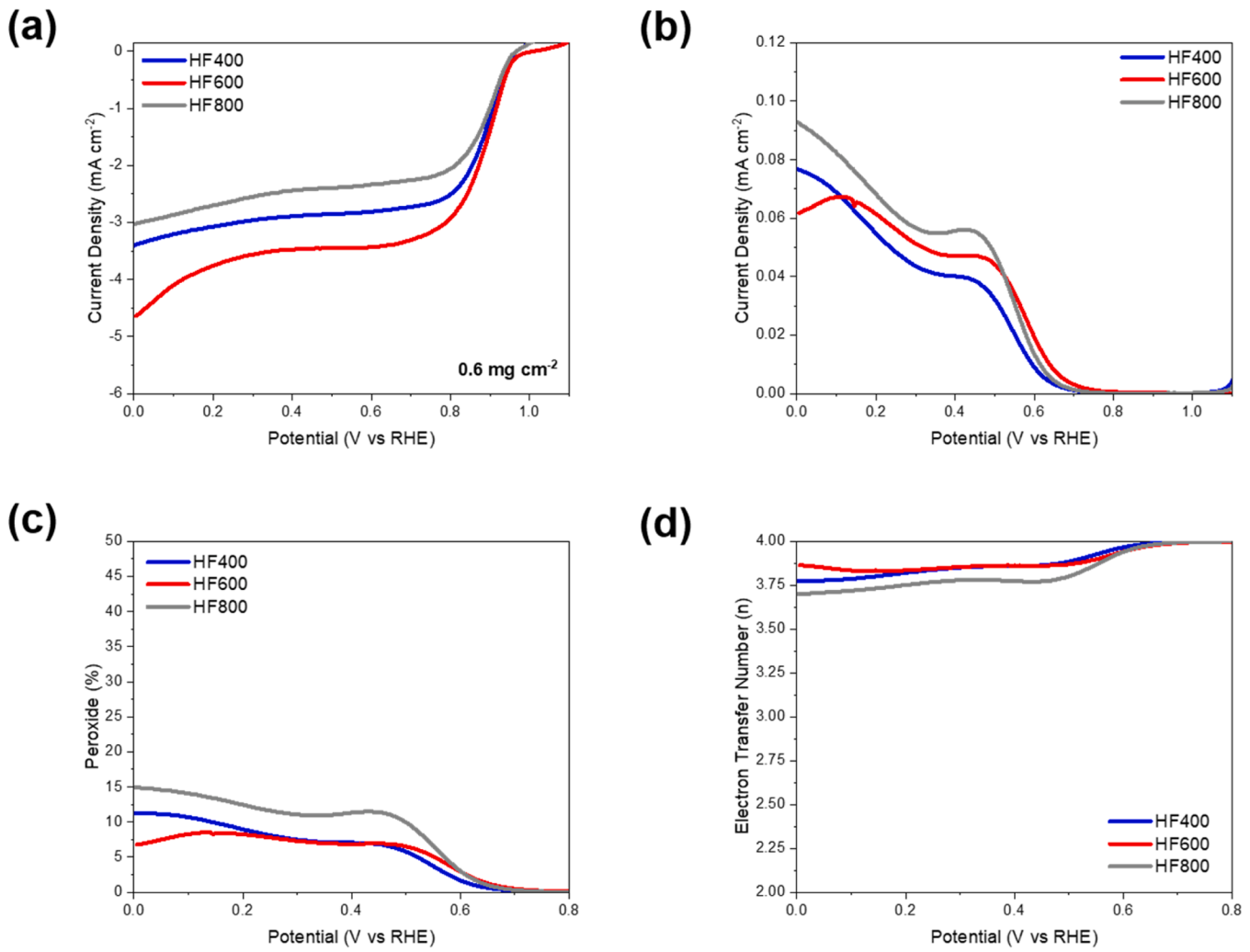

Fig. 12. RRDE measurements of the synthesized HF derived electrocatalysts in O_2-saturated 0.1 M KOH at 1600 rpm, with an electrocatalyst loading of 0.6 mg cm^{-2}. (a) LSV disk current densities at a scan rate of 5 mV s^{-1}, (b) ring current densities, (c) peroxide anion yield, and (d) the number of electrons transferred during ORR.

morphological uniformity likely enhances the mass transport and the accessibility of the catalytic sites to the reactants and guarantees that the active sites are well distributed inside the electrocatalyst, leading to improved efficiency. By contrast, the heterogeneous porous structures of the other electrocatalysts may hinder the ORR, resulting in worse electrocatalytic activities, especially in terms of peroxide production and number of transferred electrons (see Table S2).

Owing to optimum ORR performance, the sample HF600 was further tested for its stability over 2000 cycles by configuring the working electrode consisting of 0.6 mg cm^{-2} loading of sample on the glassy carbon of RDE (Figure S16). Remarkably, HF600 demonstrates adequate stability where the E_{onset} and $E_{1/2}$ remained almost comparable with a slight change in the J_{lim}, which could be due to the detachment of the sample of the continuous cycling.

Table 2
Performance of biomass-derived electrocatalysts for ORR in alkaline media.

Sample	Biomass	E_{on} (V vs RHE)	$E_{1/2}$ (V vs RHE)	Peroxide Anion (%)	Electron Transfer No (n)	Electrolyte	Ref.
HS600	Hemp Shives	0.96	0.92	< 8 %	3.8	0.1 M KOH	This work
HF600	Hemp Fibers	0.97	0.92	< 7 %	3.9	0.1 M KOH	This work
FeNC(Mg)	Lignin	0.95	0.83	-	ca. 4	0.1 M KOH	[14]
Co/NHPC-90	Hemp	-	0.82	-	-	0.1 M KOH	[29]
NSPC-800	Shrimp's Chitosan	0.95	0.85	5.9 %	3.69	0.1 M KOH	[58]
Fe_2O_3/N-PCs-850	Mulberry leaf	0.93	0.77	5 %	3.9	0.1 M KOH	[59]
Fe–N–PC	Soybean Straw	0.98	0.85	< 1 %	3.97	0.1 M KOH	[63]
RN350-Z(1–2)-1000	Legume Root Nodules	0.97	0.87	< 18.74 %	3.63>	0.1 M KOH	[64]
FeCo/N-C-Pistachio	Pistachio Shells	0.93	0.83	-	3.8	0.1 M KOH	[60]
D-MNS-A	Macadamia Nut Shell	0.87	0.75	< 13 %	3.6	0.1 M KOH	[61]
Fe-NLC-1	Lignin	1.02	0.90	2 %	ca. 4	0.1 M KOH	[65]
Fe_2O_3-CW_{1000}	Balsa Wood	0.98	0.78	< 5 %	3.8	0.1 M KOH	[66]

3.5.1. Comparison with literature

To showcase the significance and the novelty of the work, it is important to compare the electrochemical characteristics of the hemp derived electrocatalysts of this study with those recently reported in the literature. Therefore, Table 2 presents an overview of electrocatalytic activities of the best-performing electrocatalysts i.e. HS600 and HF600 in a comparison with the state-of-the-art biomass-derived electrocatalysts under similar experimental settings and, importantly, in alkaline media. In terms of the kinetic parameters, the present work stands out with higher E_{onset} (0.96–0.97 V vs RHE) and $E_{1/2}$ (0.92 V vs RHE) values which are closely comparable and even higher than the various biomass-derived electrocatalysts [25,57–62]. In fact, the values of E_{onset} and $E_{1/2}$ are more positive with respect to the commercial benchmark Pt/C (20 wt. % Pt) electrocatalysts reported in other studies [61,63]. Similarly, peroxide production is lower typically <10 %, which is positive to preserve membrane integrity inside the fuel cells during operations. This goes in accordance with the high number of electrons transferred (n = 3.8–3.9).

4. Conclusion

Hemp fibers and shives separately, as low-value waste biomass, were first utilized to produce activated char with interconnected porosity. Subsequently, the char samples acquired at different temperatures were functionalized with FePc to create monometallic electrocatalysts. These electrocatalysts exhibited defect-rich porous structures (in the mesoporous range) without any agglomeration of metallic nanoparticles as highlighted by ^{129}Xe NMR spectra. XPS analysis confirmed the presence of various nitrogen-containing active moieties and the presence of the desired Nx-Me active sites, with generally higher iron and nitrogen content in hemp fibers-derived electrocatalysts.

RRDE measurements in alkaline media, conducted with loadings of 0.2 mg cm^{-2} and 0.6 mg cm^{-2}, validated the active nature of the resulting electrocatalysts. In alkaline media, HS600 and HF600 electrocatalysts had an overall higher performance than the rest in terms of E_{on}, with values of 0.96 and 0.97 V vs RHE, respectively, and $E_{1/2}$, with value of 0.92 V vs RHE. Interestingly both HS600 and HF600 electrocatalysts achieved the lowest peroxide production yield and the highest transferred number of electrons. These results could be related to favorable morphological attributes and the coexistence of desired nitrogen moieties and the distribution of Fe-N_x active sites.

This work explores new biomass raw material, derived from industrial waste, for cost-effective development of M-N-C electrocatalysts with excellent physicochemical and electrochemical properties for ORR in AEMFC.

CRediT authorship contribution statement

Leire Caizán-Juanarena: Writing – review & editing, Writing – original draft, Methodology, Investigation, Formal analysis, Data curation, Conceptualization. **Matteo Boventi:** Writing – review & editing, Writing – original draft, Methodology, Investigation, Formal analysis, Data curation, Conceptualization. **Mohsin Muhyuddin:** Writing – review & editing, Writing – original draft, Methodology, Investigation, Formal analysis, Data curation. **Stefano Caporali:** Writing – review & editing, Writing – original draft, Methodology, Investigation, Formal analysis, Data curation. **Enrico Berretti:** Writing – original draft, Methodology, Investigation, Formal analysis, Data curation. **Alessandro Lavacchi:** Writing – review & editing, Writing – original draft, Methodology, Investigation. **Antunes Staffolani:** Data curation, Formal analysis, Investigation, Methodology, Writing – review & editing. **Michele Mauri:** Writing – original draft, Methodology, Investigation, Data curation. **Roberto Simonutti:** Writing – review & editing, Writing – original draft, Visualization, Supervision, Project administration, Methodology, Investigation, Funding acquisition, Formal analysis, Data curation, Conceptualization. **Carlo Santoro:** Writing – review & editing, Writing – original draft, Supervision, Methodology, Funding acquisition, Conceptualization.

Declaration of competing interest

The authors declare that they have no known competing financial interests or personal relationships that could have appeared to influence the work reported in this paper.

Acknowledgements

L.C.J. would like to thank Consejería de Universidad, Investigación e Innovación (Junta de Andalucía) for the PAIDI 2020 Postdoc grant and the European Social Fund for the support (ref. DOC 01168), Ministerio de Ciencia, Innovación y Universidades for the José Castillejo 2022 fellowship, and the University of Málaga for the B1 funding (ref. B1-2021_03).

This study was carried out within the MOST e Sustainable Mobility Center and received funding from the European Union Next-GenerationEU (PIANO NAZIONALE DI RIPRESA E RESILIENZA (PNRR) e MISSIONE 4 COMPONENTE 2, INVESTIMENTO 1.4 e D.D. 1033 17/06/2022, CN00000023). This manuscript reflects only the authors' views and opinions, neither the European Union nor the European Commission can be considered responsible for them. The Environmental Management Group of Univerity of Bologna (https://site.unibo.it/environmental-management-research-group/en) is acknowledged for the kind support in porosimetry analyses.

E.B. would like to acknowledge the Circular and Sustainable Made in Italy Extended Partnership (MICS) funded by the European Union Next-Generation EU (Piano Nazionale di Ripresa e Resilienza (PNRR) - Missione 4, Componente2, Investimento 1.3 - D.D. 1551.11-10-2022, PE00000004) for financial support.

C.S. and M.Mu. would like to also acknowledge the Cariplo Foundation, Call for Circular Economy through the project "Transformation of plastic waste in Electrocatalysts, Supported by exhausted gases recovery Layout" (TESLA).

M.Ma, M.B. and R.S. acknowledge MAEKO Srl for kindly providing hemp shives and fibers.

Supplementary materials

Supplementary material associated with this article can be found, in the online version, at doi:10.1016/j.electacta.2025.146094.

Data availability

Data will be made available on request.

References

[1] A.G. Olabi, T. Wilberforce, M.A. Abdelkareem, Fuel cell application in the automotive industry and future perspective, Energy 214 (2021) 118955, https://doi.org/10.1016/j.energy.2020.118955.

[2] M. Shao, Q. Chang, J.-P. Dodelet, R. Chenitz, Recent advances in electrocatalysts for oxygen reduction reaction, Chem. Rev. 116 (2016) 3594–3657, https://doi.org/10.1021/acs.chemrev.5b00462.

[3] H.A. Gasteiger, S.S. Kocha, B. Sompalli, F.T. Wagner, Activity benchmarks and requirements for Pt, Pt-alloy, and non-Pt oxygen reduction catalysts for PEMFCs, Applied Catalysis B: Environmental 56 (2005) 9–35, https://doi.org/10.1016/j.apcatb.2004.06.021.

[4] W. Wang, Q. Jia, S. Mukerjee, S. Chen, Recent insights into the oxygen-reduction electrocatalysis of Fe/N/C materials, ACS. Catal. 9 (2019) 10126–10141, https://doi.org/10.1021/acscatal.9b02583.

[5] Y. He, S. Liu, C. Priest, Q. Shi, G. Wu, Atomically dispersed metal–nitrogen–carbon catalysts for fuel cells: advances in catalyst design, electrode performance, and durability improvement, Chem. Soc. Rev. 49 (2020) 3484–3524, https://doi.org/10.1039/C9CS00903E.

[6] S.A. Mirshokraee, M. Muhyuddin, N. Pianta, E. Berretti, L. Capozzoli, J. Orsilli, F. D'Acapito, R. Viscardi, A. Cosenza, P. Atanassov, C. Santoro, A. Lavacchi, Ni-phthalocyanine derived electrocatalysts for oxygen reduction reaction and

hydrogen evolution reaction: active sites formation and electrocatalytic activity, ACS. Catal. 14 (2024) 14524–14538, https://doi.org/10.1021/acscatal.4c03814.
[7] K. Singh, F. Razmjooei, J.-S. Yu, Active sites and factors influencing them for efficient oxygen reduction reaction in metal-N coordinated pyrolyzed and non-pyrolyzed catalysts: a review, J. Mater. Chem. A 5 (2017) 20095–20119, https://doi.org/10.1039/C7TA05222G.
[8] S. Zago, L.C. Scarpetta-Pizo, J.H. Zagal, S. Specchia, PGM-free biomass-derived electrocatalysts for oxygen reduction in energy conversion devices: promising materials, Electrochem. Energy Rev. 7 (2024) 1, https://doi.org/10.1007/s41918-023-00197-3.
[9] S. Kumar, S.K. Lohan, D.S. Parihar, Biomass energy from agriculture, in: A. Rakshit, A. Biswas, D. Sarkar, V.S. Meena, R. Datta (Eds.), Handbook of Energy Management in Agriculture, Springer Nature, Singapore, 2023, pp. 181–199, https://doi.org/10.1007/978-981-19-7736-7_10-1.
[10] R. Boddula, Y.-Y. Lee, S. Masimukku, G.-P. Chang-Chien, R. Pothu, R.K. Srivastava, P.K. Sarangi, M. Selvaraj, S. Basumatary, N. Al-Qahtani, Sustainable hydrogen production: solar-powered biomass conversion explored through (Photo) electrochemical advancements, Process Safety and Environmental Protection 186 (2024) 1149–1168, https://doi.org/10.1016/j.psep.2024.04.068.
[11] L. Du, G. Zhang, X. Liu, A. Hassanpour, M. Dubois, A.C. Tavares, S. Sun, Biomass-derived nonprecious metal catalysts for oxygen reduction reaction: the demand-oriented engineering of active sites and structures, Carbon Energy 2 (2020) 561–581, https://doi.org/10.1002/cey2.73.
[12] M. Borghei, J. Lehtonen, L. Liu, O.J. Rojas, Advanced biomass-derived electrocatalysts for the oxygen reduction reaction, Advanced Materials 30 (2018) 1703691, https://doi.org/10.1002/adma.201703691.
[13] A. Sumboja, B. Prakoso, Y. Ma, F.R. Irwan, J.J. Hutani, A. Mulyadewi, M.A. A. Mahbub, Y. Zong, Z. Liu, FeCo nanoparticle-loaded nutshell-derived porous carbon as sustainable catalyst in Al-air batteries, Energy Material Advances (2021) 2021, https://doi.org/10.34133/2021/7386210.
[14] U. Sajjad, A. Sarapuu, J.C. Douglin, A. Kikas, A. Treshchalov, M. Käärik, J. Kozlova, J. Aruväli, J. Leis, V. Kisand, K. Kukli, D.R. Dekel, K. Tammeveski, Lignin-derived precious metal-free electrocatalysts for anion-exchange membrane fuel cell application, ACS. Catal. 14 (2024) 9224–9234, https://doi.org/10.1021/acscatal.4c02136.
[15] S.A. Mirshokraee, M. Muhyuddin, R. Lorenzi, G. Tseberlidis, C.L. Vecchio, V. Baglio, E. Berretti, A. Lavacchi, C. Santoro, Litchi-derived platinum group metal-free electrocatalysts for oxygen reduction reaction and hydrogen evolution reaction in alkaline media, SusMat 3 (2023) 248–262, https://doi.org/10.1002/sus2.121.
[16] A. Vazhayil, S. Ashok C, S. Majumder, A.A. Jeffery, M. Altaf, Y.-H. Ahn, N. Thomas, Orange peel derived activated carbon supported Ni–Co3O4 as an efficient electrocatalyst for oxygen evolution and reduction reaction in alkaline media, Mater. Chem. Phys. 328 (2024) 129983, https://doi.org/10.1016/j.matchemphys.2024.129983.
[17] D. Testa, G. Zuccante, M. Muhyuddin, R. Landone, A. Scommegna, R. Lorenzi, M. Acciarri, E. Petri, F. Soavi, L. Poggini, L. Capozzoli, A. Lavacchi, N. Lamanna, A. Franzetti, L. Zoia, C. Santoro, Giving new life to waste cigarette butts: transformation into platinum group metal-free electrocatalysts for oxygen reduction reaction in acid, neutral and alkaline environment, Catalysts. 13 (2023) 635, https://doi.org/10.3390/catal13030635.
[18] G. Zuccante, M. Muhyuddin, V.C.A. Ficca, E. Placidi, M. Acciarri, N. Lamanna, A. Franzetti, L. Zoia, M. Bellini, E. Berretti, A. Lavacchi, C. Santoro, Transforming cigarette wastes into oxygen reduction reaction electrocatalyst: does each component behave differently? An Experimental Evaluation, ChemElectroChem 11 (2024) e202300725 https://doi.org/10.1002/celc.202300725.
[19] D. Sieracka, J. Frankowski, S. Wacławek, W. Czekała, Hemp biomass as a raw material for sustainable development, Applied Sciences 13 (2023) 9733, https://doi.org/10.3390/app13179733.
[20] A.R. Gill, B.R. Loveys, T.R. Cavagnaro, R.A. Burton, The potential of industrial hemp (Cannabis sativa L.) as an emerging drought resistant fibre crop, Plant Soil. 493 (2023) 7–16, https://doi.org/10.1007/s11104-023-06219-9.
[21] Hemp production offers broad opportunities for farmers, industrial sectors and consumers in the European Union., (n.d.). https://agriculture.ec.europa.eu/farming/crop-productions-and-plant-based-products/hemp_en (accessed January 6, 2025).
[22] A.T.M.F. Ahmed, M.Z. Islam, M.S. Mahmud, M.E. Sarker, M.R. Islam, Hemp as a potential raw material toward a sustainable world: a review, Heliyon. 8 (2022), https://doi.org/10.1016/j.heliyon.2022.e08753.
[23] M. Tripathi, M. Sharma, S. Bala, J. Connell, J.R. Newbold, R.M. Rees, T. M. Aminabhavi, V.K. Thakur, V.K. Gupta, Conversion technologies for valorization of hemp lignocellulosic biomass for potential biorefinery applications, Sep. Purif. Technol. 320 (2023) 124018, https://doi.org/10.1016/j.seppur.2023.124018.
[24] A. Wawro, J. Batog, W. Gieparda, Chemical and enzymatic treatment of hemp biomass for bioethanol production, Applied Sciences 9 (2019) 5348, https://doi.org/10.3390/app9245348.
[25] M. Borghei, J. Lehtonen, L. Liu, O.J. Rojas, Advanced biomass-derived electrocatalysts for the oxygen reduction reaction, Advanced Materials 30 (2018) 1703691, https://doi.org/10.1002/adma.201703691.
[26] L. Marrot, K. Candelier, J. Valette, C. Lanvin, B. Horvat, L. Legan, D.B. DeVallance, Valorization of hemp stalk waste through thermochemical conversion for energy and electrical applications, Waste Biomass Valor 13 (2022) 2267–2285, https://doi.org/10.1007/s12649-021-01640-6.
[27] D. Antorán, D. Alvira, M.E. Peker, H. Malón, S. Irusta, V. Sebastián, J.J. Manyà, Waste hemp hurd as a sustainable precursor for affordable and high-rate hard carbon-based anodes in sodium-ion batteries, Energy Fuels. 37 (2023) 9650–9661, https://doi.org/10.1021/acs.energyfuels.3c01040.
[28] B. Tekin, Y. Topcu, Novel hemp biomass-derived activated carbon as cathode material for aqueous zinc-ion hybrid supercapacitors: synthesis, characterization, and electrochemical performance, J. Energy Storage 77 (2024) 109879, https://doi.org/10.1016/j.est.2023.109879.
[29] C. Zhang, J. Shu, S. Shi, J. Nie, G. Ma, Hemp derived N-doped highly porous carbon containing Co nanoparticles as electrocatalyst for oxygen reduction reaction, J. Colloid. Interface Sci. 559 (2020) 21–28, https://doi.org/10.1016/j.jcis.2019.09.064.
[30] A.H. Tkaczyk, A. Bartl, A. Amato, V. Lapkovskis, M. Petranikova, Sustainability evaluation of essential critical raw materials: cobalt, niobium, tungsten and rare earth elements, J. Phys. D: Appl. Phys. 51 (2018) 203001, https://doi.org/10.1088/1361-6463/aaba99.
[31] D.J. Paustenbach, B.E. Tvermoes, K.M. Unice, B.L. Finley, B.D. Kerger, A review of the health hazards posed by cobalt, Crit. Rev. Toxicol. 43 (2013) 316–362, https://doi.org/10.3109/10408444.2013.779633.
[32] T. Asset, P. Atanassov, Iron-nitrogen-carbon catalysts for proton exchange membrane fuel cells, Joule 4 (2020) 33–44, https://doi.org/10.1016/j.joule.2019.12.002.
[33] M. Muhyuddin, S. Mostoni, H.C. Honig, L. Mirizzi, L. Elbaz, R. Scotti, M. D'Arienzo, C. Santoro, Enhancing electrocatalysis: engineering the Fe–Nx–C electrocatalyst for oxygen reduction reaction using Fe-functionalized silica hard templates, ACS Appl. Energy Mater. 7 (2024) 11691–11702, https://doi.org/10.1021/acsaem.4c01215.
[34] Y. Lv, F. Zhang, Y. Dou, Y. Zhai, J. Wang, H. Liu, Y. Xia, B. Tu, D. Zhao, A comprehensive study on KOH activation of ordered mesoporous carbons and their supercapacitor application, J. Mater. Chem. 22 (2011) 93, https://doi.org/10.1039/C1JM12742J.
[35] M. Boventi, M. Mauri, K. Golker, J.G. Wiklander, I.A. Nicholls, R. Simonutti, Porosity of molecularly imprinted polymers investigated by 129Xe NMR spectroscopy, ACS Appl. Polym. Mater. 4 (2022) 8740–8749, https://doi.org/10.1021/acsapm.2c01084.
[36] N. Giulini, M. Muhyuddin, S. Mattiello, M. Sassi, C. Lo Vecchio, V. Baglio, E. Berretti, A. Lavacchi, E. Fazio, L. Beverina, C. Santoro, Repurposing discarded porphyrin waste as electrocatalysts for the oxygen reduction reaction, Electrochim. Acta 507 (2024) 145113, https://doi.org/10.1016/j.electacta.2024.145113.
[37] S. Liu, L. Ge, S. Gao, L. Zhuang, Z. Zhu, H. Wang, Activated carbon derived from bio-waste hemp hurd and retted hemp hurd for CO2 adsorption, Composites Communications 5 (2017) 27–30, https://doi.org/10.1016/j.coco.2017.06.002.
[38] K.V. Romanenko, J.-B. d'Espinose de Lacaillerie, O. Lapina, J. Fraissard, Is 129Xe NMR a useful technique for probing the pore structure and surface properties of carbonaceous solids? Microporous and Mesoporous Materials 105 (2007) 118–123, https://doi.org/10.1016/j.micromeso.2007.05.022.
[39] M. Boventi, M. Mauri, R. Simonutti, 129Xe: a wide-ranging NMR probe for multiscale structures, Applied Sciences 12 (2022) 3152, https://doi.org/10.3390/app12063152.
[40] M. Farina, M. Mauri, G. Patriarca, R. Simonutti, K.T. Klasson, H.N. Cheng, 129 Xe NMR studies of morphology and accessibility in porous biochar from almond shells, RSC Adv. 6 (2016) 103803–103810, https://doi.org/10.1039/C6RA18104J.
[41] A. Bifone, T. Pietrass, J. Kritzenberger, A. Pines, B.F. Chmelka, Surface study of supported metal particles by ${·}^{129}\mathrm{Xe}$ NMR, Phys. Rev. Lett. 74 (1995) 3277–3280, https://doi.org/10.1103/PhysRevLett.74.3277.
[42] E. Vismara, C. Bongio, A. Coletti, R. Edelman, A. Serafini, M. Mauri, R. Simonutti, S. Bertini, E. Urso, Y.G. Assaraf, Y.D. Livney, Albumin and hyaluronic acid-coated superparamagnetic iron oxide nanoparticles loaded with Paclitaxel for biomedical applications, Molecules. 22 (2017) 1030, https://doi.org/10.3390/molecules22071030.
[43] M. Mauri, R. Simonutti, Hyperpolarized xenon nuclear magnetic resonance (NMR) of building stone materials, Materials. (Basel) 5 (2012) 1722–1739, https://doi.org/10.3390/ma5091722.
[44] S. Brunauer, P.H. Emmett, E. Teller, Adsorption of gases in multimolecular layers, J. Am. Chem. Soc. 60 (1938) 309–319, https://doi.org/10.1021/ja01269a023.
[45] L. Yang, J. Shui, L. Du, Y. Shao, J. Liu, L. Dai, Z. Hu, Carbon-based metal-free ORR electrocatalysts for fuel cells: past, present, and future, Advanced Materials 31 (2019) 1804799, https://doi.org/10.1002/adma.201804799.
[46] K. Artyushkova, A. Serov, S. Rojas-Carbonell, P. Atanassov, Chemistry of multitudinous active sites for oxygen reduction reaction in transition metal–Nitrogen–Carbon electrocatalysts, J. Phys. Chem. C 119 (2015) 25917–25928, https://doi.org/10.1021/acs.jpcc.5b07653.
[47] S. Kabir, K. Artyushkova, A. Serov, B. Kiefer, P. Atanassov, Binding energy shifts for nitrogen-containing graphene-based electrocatalysts – experiments and DFT calculations, Surface and Interface Analysis 48 (2016) 293–300, https://doi.org/10.1002/sia.5935.
[48] Y. Chen, I. Matanovic, E. Weiler, P. Atanassov, K. Artyushkova, Mechanism of oxygen reduction reaction on transition metal–Nitrogen–Carbon catalysts: establishing the role of nitrogen-containing active sites, ACS Appl. Energy Mater. 1 (2018) 5948–5953, https://doi.org/10.1021/acsaem.8b00959.
[49] X. Ge, A. Sumboja, D. Wuu, T. An, B. Li, F.W.T. Goh, T.S.A. Hor, Y. Zong, Z. Liu, Oxygen reduction in alkaline Media: from mechanisms to recent advances of catalysts, ACS. Catal. 5 (2015) 4643–4667, https://doi.org/10.1021/acscatal.5b00524.
[50] S. Kabir, K. Artyushkova, A. Serov, P. Atanassov, Role of nitrogen moieties in N-doped 3D-graphene nanosheets for oxygen electroreduction in acidic and alkaline Media, ACS Appl. Mater. Interfaces 10 (2018) 11623–11632, https://doi.org/10.1021/acsami.7b18651.

[51] S. Hu, W. Ni, D. Yang, C. Ma, J. Zhang, J. Duan, Y. Gao, S. Zhang, Fe3O4 nanoparticles encapsulated in single-atom Fe–N–C towards efficient oxygen reduction reaction: effect of the micro and macro pores, Carbon. N. Y. 162 (2020) 245–255, https://doi.org/10.1016/j.carbon.2020.02.059.
[52] U. Tylus, Q. Jia, K. Strickland, N. Ramaswamy, A. Serov, P. Atanassov, S. Mukerjee, Elucidating oxygen reduction active sites in pyrolyzed metal–Nitrogen coordinated non-precious-metal electrocatalyst systems, J. Phys. Chem. C 118 (2014) 8999–9008, https://doi.org/10.1021/jp500781v.
[53] G. Zhong, S. Xu, L. Liu, C.Z. Zheng, J. Dou, F. Wang, X. Fu, W. Liao, H. Wang, Effect of experimental operations on the limiting current density of oxygen reduction reaction evaluated by rotating-disk electrode, ChemElectroChem. 7 (2020) 1107–1114, https://doi.org/10.1002/celc.201902085.
[54] E. Wallnöfer-Ogris, F. Poimer, R. Köll, M.-G. Macherhammer, A. Trattner, Main degradation mechanisms of polymer electrolyte membrane fuel cell stacks – Mechanisms, influencing factors, consequences, and mitigation strategies, Int. J. Hydrogen. Energy 50 (2024) 1159–1182, https://doi.org/10.1016/j.ijhydene.2023.06.215.
[55] C. Santoro, M. Kodali, S. Herrera, A. Serov, I. Ieropoulos, P. Atanassov, Power generation in microbial fuel cells using platinum group metal-free cathode catalyst: effect of the catalyst loading on performance and costs, J. Power. Sources. 378 (2018) 169–175, https://doi.org/10.1016/j.jpowsour.2017.12.017.
[56] A. Bonakdarpour, M. Lefevre, R. Yang, F. Jaouen, T. Dahn, J.-P. Dodelet, J.R. Dahn, Impact of loading in RRDE experiments on Fe–N–C catalysts: two- or four-electron oxygen reduction? Electrochem. Solid-State Lett. 11 (2008) B105, https://doi.org/10.1149/1.2904768.
[57] A. Dessalle, J. Quílez-Bermejo, V. Fierro, F. Xu, A. Celzard, Recent progress in the development of efficient biomass-based ORR electrocatalysts, Carbon. N. Y. 203 (2023) 237–260, https://doi.org/10.1016/j.carbon.2022.11.073.
[58] M.M. Mohideen, Q. Wang, S. Ramakrishna, Y. Liu, Chitosan-derived carbon sphere with self-activating behavior for stable oxygen reduction reaction in acid and alkaline media, Carbon. N. Y. 226 (2024) 119154, https://doi.org/10.1016/j.carbon.2024.119154.
[59] T. Zhang, L. Guan, C. Li, J. Zhao, M. Wang, L. Peng, J. Wang, Y. Lin, Cost-effective and facile preparation of Fe2O3 nanoparticles decorated N-doped mesoporous carbon materials: transforming mulberry leaf into a highly active electrocatalyst for oxygen reduction reactions, Catalysts. 8 (2018) 101, https://doi.org/10.3390/catal8030101.
[60] A. Sumboja, B. Prakoso, Y. Ma, F. Irwan, J. Hutani, A. Mulyadewi, M.A.A. Mahbub, Y. Zong, Z. Liu, FeCo nanoparticle-loaded nutshell-derived porous carbon as sustainable catalyst in Al-air batteries, Energy Material Advances 2021 (2021) 1–12, https://doi.org/10.34133/2021/7386210.
[61] X. Yan, Y. Jia, L. Zhuang, L. Zhang, K. Wang, X. Yao, Defective carbons derived from Macadamia Nut shell biomass for efficient oxygen reduction and supercapacitors, ChemElectroChem. 5 (2018) 1874–1879, https://doi.org/10.1002/celc.201800068.
[62] M. Wang, S. Wang, H. Yang, W. Ku, S. Yang, Z. Liu, G. Lu, Carbon-based electrocatalysts derived from biomass for oxygen reduction reaction: a Minireview, Front. Chem. 8 (2020), https://doi.org/10.3389/fchem.2020.00116.
[63] Y. Liu, M. Su, D. Li, S. Li, X. Li, J. Zhao, F. Liu, Soybean straw biomass-derived Fe–N co-doped porous carbon as an efficient electrocatalyst for oxygen reduction in both alkaline and acidic media, RSC. Adv. 10 (2020) 6763–6771, https://doi.org/10.1039/C9RA07539A.
[64] M. Hao, R. Dun, Y. Su, L. He, F. Ning, X. Zhou, W. Li, In situ self-doped biomass-derived porous carbon as an excellent oxygen reduction electrocatalyst for fuel cells and metal–air batteries, J. Mater. Chem. A 9 (2021) 14331–14343, https://doi.org/10.1039/D1TA01417J.
[65] D. Qian, X. Hu, Y. Huang, Lignin-derived Fe–N–C electrocatalyst with 3D porous structure for efficient oxygen reduction reaction, Int. J. Hydrogen. Energy 89 (2024) 1003–1011, https://doi.org/10.1016/j.ijhydene.2024.09.308.
[66] W. Miao, S. Li, X. Cao, E. Lv, H. Yu, X. Zhang, X. Dong, Wood-derived porous carbon supported γ-Fe2O3 nanoparticles as efficient catalyst for oxygen reduction reaction, Appl. Surf. Sci. 604 (2022) 154471, https://doi.org/10.1016/j.apsusc.2022.154471.